

# Differentially Rotating White Dwarfs I: Regimes of Internal Rotation

Pranab Ghosh<sup>1,3</sup> and J. Craig Wheeler<sup>2</sup>

Received \_\_\_\_\_; accepted \_\_\_\_\_

---

<sup>1</sup>Department of Astronomy & Astrophysics, Tata Institute of Fundamental Research, Mumbai 400 005, India

<sup>2</sup>Department of Astronomy, University of Texas at Austin, Austin, Texas 78712

<sup>3</sup>Current Address: 10/1 Murari Pukur Lane, Kolkata 700 067, India

## ABSTRACT

Most viable models of Type Ia supernovae (SN Ia) require the thermonuclear explosion of a carbon/oxygen white dwarf that has evolved in a binary system. Rotation could be an important aspect of any model for SN Ia, whether single or double degenerate, with the white dwarf mass at, below, or above the Chandrasekhar limit. *Differential rotation* is specifically invoked in attempts to account for the apparent excess mass in the super-Chandrasekhar events. Some earlier work has suggested that only uniform rotation is consistent with the expected mechanisms of angular momentum transport in white dwarfs, while others have found pronounced differential rotation. We show that if the baroclinic instability is active in degenerate matter and the effects of magnetic fields are neglected, both nearly-uniform and strongly-differential rotation are possible. We classify rotation regimes in terms of the Richardson number,  $Ri$ . At small values of  $Ri \leq 0.1$ , we find both the low-viscosity Zahn regime with a non-monotonic angular velocity profile and a new differential rotation regime for which the viscosity is high and scales linearly with the shear,  $\sigma$ . Employment of Kelvin-Helmholtz viscosity alone yields differential rotation. Large values of  $Ri \gg 1$  produce a regime of nearly-uniform rotation for which the baroclinic viscosity is of intermediate value and scales as  $\sigma^3$ . We discuss the gap in understanding of the behavior at intermediate values of  $Ri$  and how observations may constrain the rotation regimes attained by nature.

*Subject headings:* physical processes: diffusion – binaries: close – stars: evolution – supernovae: general – stars: white dwarfs

## 1. Introduction

Although the basic explosion mechanism of supernovae of Type Ia (henceforth SN Ia) has been established to be the thermonuclear combustion of degenerate C/O white dwarfs (henceforth WD), many aspects of the progenitor systems of remain to be understood. Nearly all viable progenitor models involve mass transfer in binary systems (Howell 2011; Wang & Han 2102; Maoz, Mannucci & Nelemans 2014; but see Chiosi et al. 2014). One idea is the initiation of carbon ignition as the mass approaches the classical Chandrasekhar limit of stability,  $M_{\text{Ch}} \approx 1.44M_{\odot}$ , for non-rotating WDs by means of accretion in a binary system. This classic model is most closely associated with mass transfer from a non-degenerate companion, the single-degenerate (SD) scenario. Variations on this theme allow for explosions with less than  $M_{\text{Ch}}$  when accretion of helium from a companion leads to the accumulation of an explosive degenerate layer of helium on top of the C/O core that generates compression waves that can trigger a central carbon detonation (Fink et al. 2010; Woosley & Kasen 2011; Shen & Moore 2014). This might occur by accretion from a non-degenerate companion, or from a degenerate companion in one variety of the double-degenerate (DD) scenario. Other DD models involve the tidal disruption of one WD, thus adding mass to the other, resulting in explosion (Dan et al. 2014), or the violent merger or collision of two WDs (Pakmor et al. 2012; Kushnir et al. 2013). The DD scenarios typically invoke WDs with mass less than  $M_{\text{Ch}}$ , but the total mass might exceed this amount. Other scenarios manifested in either the SD or DD context involve spinning up a WD until it is rotationally supported, with a mass exceeding  $M_{\text{Ch}}$ , the explosion being postponed until sufficient angular momentum is lost from the star. These are loosely called *spin-up/spin-down* models (Yoon & Langer 2005; Di Stefano et al. 2011; Justham 2011; Tornambe & Piersante 2013). In these models, the central density rises to the point of carbon ignition because angular momentum is lost, not because mass is gained. Yet another variation invokes the merger of a WD with a stellar core in the context of common-envelope

evolution (Livio & Riess 2003; Ilkov & Soker 2013).

In the violent merger models, the explosion occurs so quickly that an issue of the quasi-static rotational state of the WD does not arise, but in most models the physical context requires the accumulation of mass and angular momentum, and hence that the WD should rotate. The rotational state is ignored in many models of the progenitor evolution and explosion, including many computationally-demanding multi-dimensional models; however, it is obvious that, in the absence of a specific mechanism to lose angular momentum, it must accumulate.

A generic question that persists throughout the various SN Ia progenitor models is how the internal rotation profile of the accreting WD influences the essential dynamical and secular processes that operate in SN Ia progenitor environments. One basic influence of the internal rotation has been known now for four to five decades, viz., that (a) uniform rotation can increase the maximum mass of stable WDs above the Chandra limit by only about 3 to 4 percent, and (b) differential rotation can increase this maximum mass substantially, exceeding the Chandra limit by factors of up to  $\sim 2 - 3$ , and so resulting in maximum WD masses up to  $\sim (3 - 4)M_{\odot}$  (see Ostriker & Bodenheimer 1968 and references therein). We shall henceforth refer to  $M_{\text{Ch}}$  as the “Chandra limit,” and WDs with masses above this limit as “Super-Chandra.”

Most typical SN Ia are consistent with explosion at  $M_{\text{Ch}}$  (but see Scalzo et al. 2014). Polarization observations suggest that most typical SN Ia may not rotate significantly, but that subluminous events (SN 1991bg-like) may do so (Patat et al. 2012). Observations of some very bright SN Ia have led to inferred values of the ejecta mass and hence the mass of the pre-SN WD in the range  $(2.1 - 2.8) M_{\odot}$ . Examples are SN 2003fg, SN 2006gz, SN 2007if, SN 2009dc (Howell et al. 2006; Hicken et al. 2007; Yamanaka et al. 2009; Scalzo et al. 2010; Silverman et al. 2011; Taubenberger et al. 2011). These masses are

much in excess of  $M_{\text{Ch}}$ , and possible implications for the internal rotation of the pre-SN WD have been widely discussed. In this context, one may ask what evolutionary pathway would lead to a WD in a slowly-rotating state, and so in a slightly Super-Chandra condition, as opposed to a pathway that would lead to a rapidly and differentially rotating WD in a substantially Super-Chandra condition. If the WD rotates rapidly, then issues also arise about the onset of bar-mode instabilities that might affect the onset of the explosion and the subsequent dynamics.

In this paper, we focus on clarifying the origins of the different regimes of internal rotation that can exist inside accreting WDs. We consider WDs without strong, permanent magnetic fields. Accordingly, all angular-momentum transport processes considered here are necessarily described by viscosities generated only by non-magnetic mechanisms, e.g., hydrodynamic mechanisms such as Kelvin-Helmholtz and baroclinic instabilities, and secular mechanisms such as the Zahn instability (Zahn 1992). We formulate these viscosities with the aid of well-known prescriptions given in the literature. We thus describe angular-momentum transport inside accreting WDs in terms of the standard angular-momentum transport equation applied in a background WD model, which is pre-specified (§2, §3). We apply boundary conditions at the WD surface to describe the deposition of angular momentum by accreting matter. For low-viscosity (Zahn) transport (§4), we recover the differential rotation profile found earlier (Saio & Nomoto 2004). For high-viscosity transport, which includes viscosities due to both Kelvin-Helmholtz and baroclinic instabilities, we find both (a) the nearly-uniform rotation profile found earlier (Saio & Nomoto 2004; Piro 2008), and, (b) a new, differential rotation profile, which is qualitatively similar to the inner parts of the differential rotation profile found earlier for viscosity due to Kelvin-Helmholtz instability alone (Yoon & Langer 2004), but different in detail. All of the above regimes of rotation appear to be self-consistent, corresponding to different viscosities and different regimes of operation in terms of the Richardson number.

All regimes described have profiles of specific angular momentum (henceforth  $\ell$ -profile) that increase monotonically outward, as they must to be Rayleigh-stable, but the profile of the angular velocity,  $\Omega$ , (henceforth the  $\Omega$ -profile) can have a maximum inside the WD, from which it decreases both outward to the surface and inward to the center. A general and comparative discussion of these rotation profiles are given in §5, §6 and §7. A discussion, our conclusions and the prospects for future work are given §8.

## 2. Angular Momentum Transport Mechanisms

Mechanisms of angular momentum transport inside rotating stars can be classified into two general types, viz., (a) those that transport angular momentum in the  $\hat{\mathbf{r}}$ -direction, often called the *vertical* direction, the direction of local gravity, and (b) those that transport angular momentum in the  $\hat{\theta}$ -direction, often called the *horizontal* direction. The angular momentum is about the stellar rotation axis of the star, defined as the  $\hat{\mathbf{z}}$ -direction, or equivalently the  $\hat{\phi}$ -direction, in this coordinate system. Our concern in this work on accreting WDs is primarily with mechanisms of the first type, as these determine the internal rotation profile. Mechanisms of the second type work through processes such as Eddington-Sweet (henceforth ES) meridional circulation, and the Goldreich-Schubert-Fricke (henceforth GSF) instability, the primary influence of which is on the distribution of angular velocity/momentum in the meridional plane and along the  $\hat{\mathbf{z}}$ -axis (*i.e.*,  $\Omega(z)$ ).

We describe the mechanisms of vertical or  $\hat{\mathbf{r}}$ -transport of angular momentum in this section, and refer to horizontal or  $\hat{\theta}$ -transport only briefly at appropriate places. Vertical transport mechanisms involve turbulent viscosities that can be of two basic kinds: (a) those that are generated by hydrodynamical instabilities that grow on short, dynamical timescales, *e.g.*, the Kelvin-Helmholtz instability (henceforth KHI) and the baroclinic instability (henceforth BCI), and are generally high, and (b) those that are generated

by secular instabilities that grow on long, thermal timescales, e.g., the Zahn instability (henceforth ZI), and are generally low. We now discuss these two types of instabilities.

## 2.1. Hydrodynamic Instabilities and Viscous Transport

Among the best-known and most-studied hydrodynamic instabilities that grow on dynamical timescales  $\sim \Omega^{-1}$  are KHI and BCI. The former occurs when there is a (vertical) gradient in  $\Omega$ , and the latter when isobaric and isodensity surfaces do not coincide, as is the case when hydrostatic balance has to be maintained under differential rotation.

### 2.1.1. Kelvin-Helmholtz instability (KHI)

A vertical gradient in the angular velocity, as measured by the shear

$$\sigma \equiv \frac{\partial \Omega}{\partial \ln r}, \quad (1)$$

causes KHI when this shear is sufficiently strong to overcome the stabilizing effect of stratification as measured by the Brunt-Väisälä frequency,  $N$ , given by

$$N^2 \equiv \frac{g\delta}{H_p} \left[ \nabla_{\text{ad}} - \left( \frac{d \ln T}{d \ln P} \right) \right]. \quad (2)$$

In Equation (2),  $\delta \equiv -(\partial \ln \rho / \partial \ln T)_P$ ,  $H_p$  is the pressure scale height, and  $\nabla_{\text{ad}} \equiv (\partial \ln T / \partial \ln P)_{\text{ad}}$  is the adiabatic temperature gradient, the second term in the square brackets being the actual temperature gradient at the relevant point inside the star. We neglect the effect of composition gradients. The criterion for the onset of KHI is expressed in terms of the Richardson number  $\text{Ri}$ , which is defined as

$$\text{Ri} \equiv \frac{N^2}{\sigma^2}, \quad (3)$$

and which compares destabilizing shear with stabilizing buoyancy. When  $Ri$  falls below a critical value, which is widely taken to be  $1/4$ , KHI sets in. We shall adopt this critical value of the Richardson number throughout our work here.

KHI leads to a turbulent viscosity,  $\nu_{KH}$ , that can be formulated (Fujimoto 1993; Saio & Nomoto 2004; Piro 2008) as:

$$\nu_{KH} = \begin{cases} \frac{\sqrt{1-4Ri}}{2\sqrt{Ri}} H_p^2 N & Ri < 1/4 \\ 0 & Ri > 1/4. \end{cases} \quad (4)$$

This formulation has been used widely in the literature. An alternative formulation by (Heger et al. 2000; Yoon & Langer 2004) has also been used widely. It is given by:

$$\nu_{KH} = \begin{cases} (1 - 4Ri)^2 H_p^2 \Omega_K(r) & Ri < 1/4 \\ 0 & Ri > 1/4. \end{cases} \quad (5)$$

Here,  $\Omega_K(r) \equiv \sqrt{GM_r/r^3}$ , is the local Keplerian frequency inside the star and,  $M_r$  is the mass interior to radius  $r$ . We use both formulations in this work and do not find significant differences in the final results.

### 2.1.2. Baroclinic instability (BCI)

Surfaces of constant pressure and density may no longer coincide when hydrostatic equilibrium is maintained under differential rotation. Their misalignment causes BCI, the characteristics of which depend on both the Richardson number,  $Ri$ , introduced above, and a critical baroclinic Richardson number,  $Ri_{BC}$ , given by

$$Ri_{BC} \equiv 4 \left( \frac{r}{H_p} \right)^2 \frac{\Omega^2}{N^2}, \quad (6)$$

above which Coriolis forces limit the scale of the horizontal perturbations and so reduce the strength of the BCI somewhat.



BCI leads to a turbulent viscosity,  $\nu_{\text{BC}}$ , which has been given (Fujimoto 1993; Saio & Nomoto 2004; Piro 2008) as:

$$\nu_{\text{BC}} = \begin{cases} \frac{1}{3\text{Ri}^{1/2}} H_p^2 \Omega & \text{Ri} < \text{Ri}_{\text{BC}} \\ \frac{\text{Ri}_{\text{BC}}}{3\text{Ri}^{3/2}} H_p^2 \Omega & \text{Ri} \gg \text{Ri}_{\text{BC}}. \end{cases} \quad (7)$$

We use the prescription of Equation (7) in this work.

Angular momentum transport by BCI-generated viscosity for accreting degenerate stars has been studied by Fujimoto (1993), and detailed results for accreting WDs with BC viscosity included have been obtained by Saio & Nomoto (2004) and by Piro (2008). The work of Yoon & Langer (2004) is relevant in this context for having excluded BCI. We have included here both KH and BC viscosities (*i.e.*,  $\nu_{\text{KH}}$  and  $\nu_{\text{BC}}$ ), in order to have a complete discussion of all possible rotation regimes found so far. The rotation regime found by Yoon & Langer (2004), who included only the KH viscosity among the hydrodynamic ones, together with the secular Zahn viscosity and processes like the ES circulation and the GSF instability, is described in §6. The inclusion of the BCI yields the result that there are two asymptotic, disparate rotation regimes.

Although the overall prescription for the baroclinic viscosity is customarily given a single label BC, we see from Equation (7) that there are two different asymptotic regimes depending on the Richardson number, Ri. The actual viscosities are quite *different* in the two regimes, with different scalings. According to Equation (7), the BC viscosity,  $\nu_{\text{BC}}$ , scales with the Richardson number Ri as  $\text{Ri}^{-1/2}$  in the regime of small Ri, while it scales as  $\text{Ri}^{-3/2}$  in the regime of large Ri. Since Ri scales with the shear as  $\text{Ri} \propto \sigma^{-2}$ , we see that  $\nu_{\text{BC}}$  scales as  $\sigma$  in the small Ri regime, but as  $\sigma^3$  in the regime of large Ri. The addition of the KH viscosity to the BC viscosity does not change these scalings significantly, since  $\nu_{\text{KH}}$  also scales with Ri roughly as  $\text{Ri}^{-1/2}$  (Equation (4)) in the small Ri regime while  $\nu_{\text{KH}}$  vanishes in the regime of high Ri-values. Omission of the BC viscosity yields a regime dominated

by the KH viscosity. This regime is roughly comparable to the small Ri BC regime and corresponds only to differential rotation.

From these considerations, we see that in the presence of the BCI the viscous stress,  $\tau = \nu\sigma$ , scales *nonlinearly* with the shear in the regimes of both small and large Ri, with  $\tau \propto \sigma^2$  in the small Ri regime and  $\tau \propto \sigma^4$  in the large Ri regime. This difference leads to a duality in the rotation profiles, essentially solid body and substantially differential, even with the same initial and boundary conditions, depending on the effective value of Ri that in turn depends on the shear in the self-consistent solution.

In practice, these two different regimes were reproduced by implementing Equation (7) in different, but formally equivalent, ways in the two different regimes. One set of solutions began with no rotation, a given set of boundary conditions and  $\text{Ri} \ll 1$ . This formulation evolved (in *MATLAB*) a differential rotation solution, new to this work, in which both the KH and BC viscosities contributed. This solution remained in the small Ri regime, specifically  $\text{Ri} \sim 10^{-2}$ , where the viscosity scales as  $\sigma$  and  $\tau$  scales as  $\sigma^2$  (§4.2). The second formulation again adopted Equation (7), but recast in terms of the variable  $1/\text{Ri}$ , which is a small quantity in the regime of large Ri. Solving the same equations with the same boundary conditions but beginning the evolution with  $1/\text{Ri} \ll 1$  evolved a solution that, after short transient phase, attained and remained in a state of nearly solid-body rotation (§4.1) in the regime of large Ri,  $\text{Ri} \sim 10^6$ , with viscosity scaling as  $\sigma^3$ , and  $\tau$  scaling as  $\sigma^4$ . This solution was dominated by the BC viscosity and had negligible contribution from the KH viscosity. This procedure is sufficient to establish that Equation (7) supports at least two very different, self-consistent, rotation states.

The question of how the solutions evolve for the large range of intermediate values of Ri with yet different scalings with Ri and  $\sigma$  remains open. Omitting BCI, the formulation of Yoon & Langer (2004) is dominated by the KH viscosity in the inner regions and

corresponds to  $Ri$  very slightly below 0.25 in the inner regions of their models, near the low  $Ri$  regime as we define it here (§6). Uniqueness theorems say that the solution in each power-law limit,  $\nu_{BC} \propto \sigma$  and  $\nu_{BC} \propto \sigma^3$  is unique but do not constrain the behavior in intermediate regimes. We return to a discussion of these multiple solutions in §7 and §8.

## 2.2. Secular Instability and Viscous Transport

Even when stable stratification prevents dynamical instabilities, secular instabilities are still possible if there is sufficiently strong thermal diffusion that reduces the buoyancy force through radiative leakage. This phenomenon is described in terms of the Péclet number,  $Pe$ , which in this context is essentially the ratio of the rate of advection of momentum by the turbulent flow to the rate of thermal diffusion. The Péclet number is given for this particular problem by  $Pe \equiv vl/K$ , where  $v$  and  $l$  are respectively the eddy velocity and the size of turbulent eddies, and  $K$  is the thermal diffusivity. Thermal diffusion modifies the criterion for the onset of instability from  $Ri < 1/4$  to  $Ri \times Pe < 1/4$ .

The resultant secular instability, *i.e.*, the Zahn instability (ZI) leads to a turbulent viscosity,  $\nu_Z$ , that was calculated by Zahn (1992), and can be expressed as:

$$\nu_Z = \frac{2}{45} \frac{K}{Ri}. \quad (8)$$

Here,  $K \equiv 4acT^3/(3\kappa\rho^2C_p)$  is the thermal diffusivity. We use the above prescription for ZI viscosity in this work.

## 3. Angular Momentum Transport Inside White Dwarfs

In this work, we describe angular momentum transport inside accreting WDs by solving the transport equation in the background of a WD model with specified structure, thus

neglecting the effect of changing rotation on WD structure. We adopt this “toy” approach here for the purpose of clarifying the possible basic regimes of rotation profiles in accreting WDs. We do emphasize at this point that the effects of accretion are explicitly taken into account in our work by (a) keeping track of the changes in the mass and radius of the white dwarf as a result of accretion, as described below, and, (b) representing the inward transport of angular momentum by the inward motion of mass-shells in an accreting, contracting WD by a suitable “advection” term, as explained below and detailed in Appendix A.

The equation for angular momentum transport inside the WD can be expressed as

$$\frac{\partial}{\partial t} [r^2 \Omega] = \frac{1}{4\pi \rho r^2} \frac{\partial \Sigma}{\partial r}. \quad (9)$$

Here,  $\Sigma(r, t)$  is the total rate of angular momentum transport, through radius  $r$  at time  $t$ , i.e., the total torque at that radius and time. If this transport were entirely viscous, the rate would simply be  $\Sigma = 4\pi \rho \nu r^4 \partial \Omega / \partial r$ ; however, accreting WDs contract in response to their increase in mass. Consequently, each mass shell moves inward, carrying angular momentum with it. This behavior constitutes, in effect, a slow, inward advection of angular momentum through the WD on the accretion timescale (Yoon & Langer 2004). This advection is automatically taken into account if one recalculates the WD model at each step as mass and angular momentum accretion proceeds. Since we are working here with a background WD structure unaffected by changing rotation, we have to account for this advection effect explicitly. This is easily done, as we do take into account the contraction of the WD as it accretes mass, as described below. We have chosen the term “advection” for this effect to stress that this part of the transport is actually due to the slow inward motion of mass shells (in Eulerian co-ordinates) as an accreting white dwarf adjusts its internal structure, and not due to viscosity. Alternatively, if we visualize the situation in terms of Lagrangian co-ordinates, we can look upon this effect as being due to local conservation of angular momentum. We emphasize that if we define a formal advection velocity  $v_r$  (see below) for

this effect, it will be much smaller than the velocities that occur, *e.g.*, in advective accretion disks.

We now model the above effect in a straightforward manner in terms of a very slow, inward flux of matter through the WD at a rate  $\dot{M}(r, t)$ , which depends on the Eulerian radius  $r$  and the time  $t$ . We note first that we can express this slow advection as  $\dot{M}(r, t) = 4\pi r^2 \rho(r, t) v_r(r, t)$  to define a formal advection velocity  $v_r(r, t)$ , which is actually determined by the slow contraction of the WD as its mass increases due to accretion, expressed through the mass-radius relation  $R_{\text{WD}} = R_{\text{WD}}(M_{\text{WD}})$ , with  $R_{\text{WD}}$  decreasing as  $M_{\text{WD}}$  increases.

Power-law prescriptions,  $R_{\text{WD}} \sim M_{\text{WD}}^{-s}$ , have been widely used as approximations to numerical results for mass-radius relations obtained from detailed models. For low-mass WDs, the non-relativistic result  $s = 1/3$  holds well, while the power steepens as the Chandra limit is approached. As necessary, we have considered in the rest of this work both the non-relativistic limit of  $s$  and  $s$ -values  $\sim 1$  inferred from numerical WD models in the literature (Yoon & Langer 2004; Saio & Nomoto 2004).

To proceed further, we require a prescription for the contraction of the interior mass-shells as the whole WD contracts. We describe our prescription in Appendix A, where we show that the advection rate,  $\dot{M}(r, t)$ , can be reasonably approximated by a relation of the form

$$\dot{M}(r, t) \approx M_r \frac{\dot{M}_{\text{WD}}}{M_{\text{WD}}}, \quad (10)$$

where  $\dot{M}_{\text{WD}}$  is the mass accretion rate onto the WD. With this term included, the complete expression for the angular momentum transport rate, or the total torque, becomes

$$\Sigma = 4\pi \rho \nu r^4 \frac{\partial \Omega}{\partial r} + \dot{M}(r, t) r^2 \Omega, \quad (11)$$

with  $\dot{M}(r, t)$  given by Equation(10).

The equation for angular momentum transport inside the WD is obtained by combining Equations (9), (10), and (11). We then change the dependent variable to the specific angular momentum,  $\ell \equiv \Omega r^2$ , and the independent variable to the mass co-ordinate,  $M_r$ , which is related to the radial co-ordinate,  $r$ , through  $dM_r = 4\pi\rho r^2 dr$ . The final result is:

$$\frac{\partial \ell}{\partial t} = \frac{\partial}{\partial M_r} \left[ 4\pi\rho r \nu \left( 4\pi\rho r^3 \frac{\partial \ell}{\partial M_r} - 2\ell \right) + \frac{M_r \ell}{t_{ac}} \right]. \quad (12)$$

Here,  $t_{ac} \equiv M_{WD}/\dot{M}_{WD}$  is the accretion timescale.

We solve Equation (12) numerically for the various types of viscosities described above. For the background WD structure in which this transport occurs, we adopt the numerical WD models supplied to us by Montgomery (2010). The initial model, on which accretion begins, is a C/O-core WD described by the following parameters: a mass of  $M_{WD} = 1.2M_{\odot}$ , an effective surface gravity (in cgs units) of  $\log g = 9.022$ , and an effective surface temperature of  $T_{eff} = 1.2 \times 10^4$  K. The model has an appropriate gradient in the C/O ratio in the core, and there are layers of He and H on top of this core. As accretion proceeds, the WD contracts according to scheme described above, which is reflected in the outer boundary condition indicated below.

For our numerical solutions, we need appropriate initial conditions. We also need appropriate boundary conditions at the center and surface of the accreting WD. For the former, we have taken WDs that are nonrotating initially. For the latter, consider the center of the star first, where the boundary condition we apply is  $\ell_{cent} = 0$  in all cases, remembering that the transport equation (Equation (12)) is formulated in terms of  $\ell$ . We emphasize here that the angular velocity at the center,  $\Omega_{cent}$ , is not directly constrained in our solutions. Rather, it evolves along with the solution throughout the star according to the particular prescription for the viscosity. Now consider the surface of the star, where we have explored the effects of applying the two types of boundary condition suggested previously in the literature. These are: (1) the boundary condition of Saio & Nomoto

(2004), (henceforth referred to as the *SN boundary condition*), wherein the angular velocity at the surface of the WD is set to the *current* Keplerian value  $\Omega_K(R_{\text{WD}})$  there, and, (2) the boundary condition of Yoon & Langer (2004), (henceforth referred to as the *YL boundary condition*), wherein each element of accreted mass  $\Delta M$  deposits an amount of angular momentum on the WD that is (a)  $\Delta M \ell_K(R_{\text{WD}})$  if the surface angular velocity  $\Omega(R_{\text{WD}})$  of the WD is less than  $\Omega_K(R_{\text{WD}})$ , and (b) zero if  $\Omega(R_{\text{WD}}) \geq \Omega_K(R_{\text{WD}})$ . Here,  $\ell_K(R_{\text{WD}}) \equiv \Omega(R_{\text{WD}}) R_{\text{WD}}^2$  is the specific angular momentum in a Keplerian orbit at  $R_{\text{WD}}$ . We emphasize that quantities such as  $\ell_K(R_{\text{WD}})$  and  $\Omega_K(R_{\text{WD}})$  are understood here to be the *current* values, corresponding to the current values of  $M_{\text{WD}}$  and  $R_{\text{WD}}$  during the process of accretion.

Although the SN and YL boundary conditions work with the same or closely related variables, their stipulations are not exactly the same. We explore the effects of SN and YL boundary conditions in our work, using a simple version of the latter condition adequate for our purposes, which we describe in Appendix B. We find only minor differences in the final outcome. Where the differences are negligible, we quote only one result.

#### 4. Regimes of Internal Rotation for Hydrodynamic Viscosities

We now present the internal rotation profiles for the viscosities generated by hydrodynamic instabilities, *i.e.*, KHI and BCI. With both KH and BC viscosities included in our calculations, we find two regimes of rotation as sketched in §2.1.2, *viz.*, (a) nearly-uniform rotation, and, (b) strongly differential rotation. The former regime has been discussed earlier (Saio & Nomoto 2004; Piro 2008). We consider each regime in turn.

#### 4.1. Nearly-uniform Rotation

The regime of nearly-uniform rotation corresponds to the asymptotic regime of large  $\text{Ri}$  ( $\text{Ri} \sim 10^6$  in our solutions),  $\nu_{\text{BC}} \propto \sigma^3$  and  $\nu_{\text{KH}} = 0$  described in §2.1.2. The solution is illustrated in Figure 1. The left panel is a 3-D surface plot of the evolution of the  $\Omega$ -profile as accretion proceeds, while the right panel shows this evolution as stacked profiles in a 2-D plot as time elapses, the topmost curve giving the final time-step. Note that the mass co-ordinate for the profiles in this figure, and all subsequent evolutionary figures in this work, is  $M_r/M_{\text{WD}}$ , with  $M_r$  as defined earlier, and  $M_{\text{WD}}$  the current mass of the WD. Also note that time axis is marked in this figure in units of the accretion timescale as defined earlier, which is much longer than the viscous timescale for the high KH and BC viscosities (see §7). Evolution of the  $\Omega$ -profile in this case is basically the increase of this nearly-uniform  $\Omega$ -value as accretion proceeds and the WD contracts.

In practice, our solutions in this regime start with no rotation. As soon as angular momentum is added by means of a boundary condition, strong gradients, and hence finite viscosities, are temporarily generated in the outer layers. The initially large viscosity quickly leads to nearly solid-body rotation with lower viscosity and slightly, but monotonically, increasing angular velocity with radius. The viscosity in these solutions is  $\nu_{\text{BC}} \sim 10^8 \text{ cm}^2\text{s}^{-1}$ , which we label an *intermediate viscosity*, in contrast with other solutions described below. We emphasize that, for this regime as well as that of strong differential rotation described in the next subsection, the angular momentum transport equation was always solved self-consistently by evaluating Equation 7 according to the regime of locally large or small  $\text{Ri}$  at each location at a given time. We also note that the “simple” solid-body solution described in this subsection is not possible in a formulation that neglects the BCI and hence is dominated by the KHI.



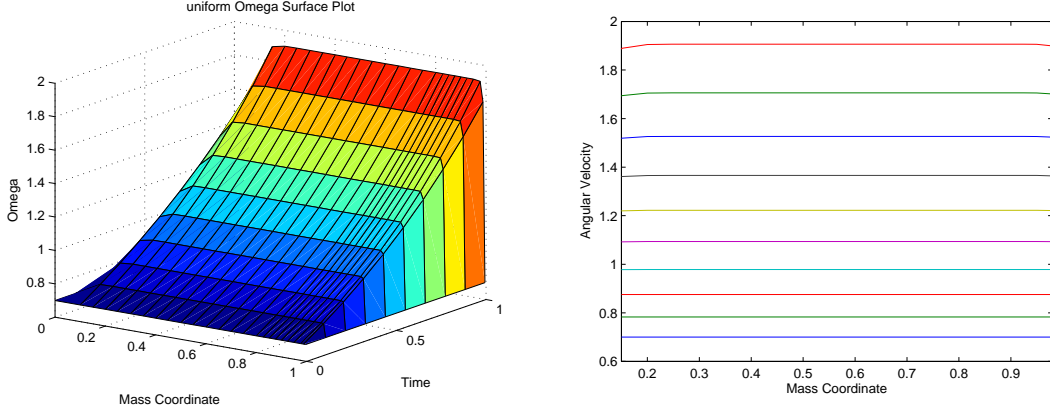


Fig. 1.— *Evolution of the angular velocity profile (in units of  $s^{-1}$ ) in the nearly-uniform rotation case with KH and BC viscosities. The time axis is marked in units of the accretion timescale. Left Panel: 3-D surface plot. Right Panel: Stacked profiles in a 2-D plot, wherein the profiles at various time-steps from the left panel are color coded, with time going up vertically.*

## 4.2. Strongly Differential Rotation

We find that strong differential rotation is also possible when viscous transport includes both KH and BC viscosities or either viscosity prescription alone. The regime of strong differential rotation corresponds to the asymptotic regime of small  $Ri$  where both  $\nu_{KH}$  and  $\nu_{BC}$  scale approximately proportionally to  $\sigma$  as described in §2.1.2. We find the effective viscosity in this regime to be  $10^{15}$  to  $10^{16}$   $cm^2s^{-1}$  (see Figure 6 below) that we label a regime of *high viscosity*. A typical example is shown in detail in Figures 2, 3, 4, and 5. In each figure, the left panel displays in a 3-D surface plot the evolution of the  $\Omega$ -profile as accretion proceeds. *The time axis is marked in these figures in units of the viscous timescale, in order to study how the profile “heals” to an asymptotic form on this timescale, and how that form evolves as accretion proceeds on a much longer timescale.* The right panel of the same figure shows the same evolution as stacked profiles in a 2-D plot as time

elapses, the topmost curve giving the final time-step.

We first explore the effect of SN boundary condition. Figure 2 shows the approach to the asymptotic state, wherein we follow the evolution to a maximum time  $t_{max} = 4$  in units of the viscous time. On the 2D plot in the right panel, the results are displayed in 10 equal steps over the time span 0 to  $t_{max}$ , the topmost curve corresponding to  $t_{max}$ .

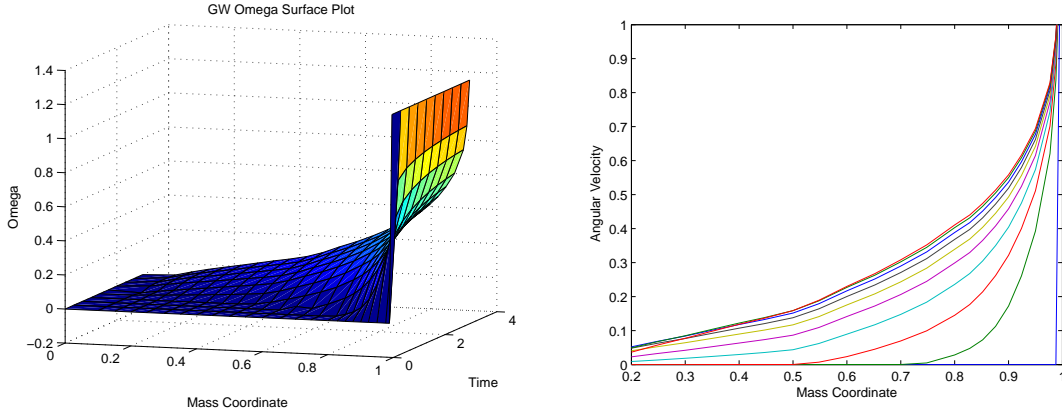


Fig. 2.— *Evolution of the angular velocity profile (in units of  $s^{-1}$ ) in the differential rotation case with KH and BC viscosities, and SN boundary condition (see text). The time axis is marked in units of the viscous timescale, the maximum time  $t_{max}$  being 4 in these units. Left Panel: 3-D surface plot. Right Panel: Stacked profiles in a 2-D plot, wherein the profiles at 10 equal time-steps are color coded, with time going up vertically.*

We show longer evolution of this profile in Figure 3, where we increase  $t_{max}$  to 500 in the same units. On the 2D plot in the right panel, the results are displayed in 10 equal steps over the time span 0 to  $t_{max}$ , the topmost curve corresponding to  $t_{max}$ . We see that the approach to the asymptotic profile is rapid, attaining it practically within the first time-step. Hence the profiles are almost indistinguishable from one another in the 2D plot.

We show even longer evolution of this profile in Figure 4, where we increase  $t_{max}$  to 50,000 in the same units to confirm the result. We do not repeat the 2D plot in this case,

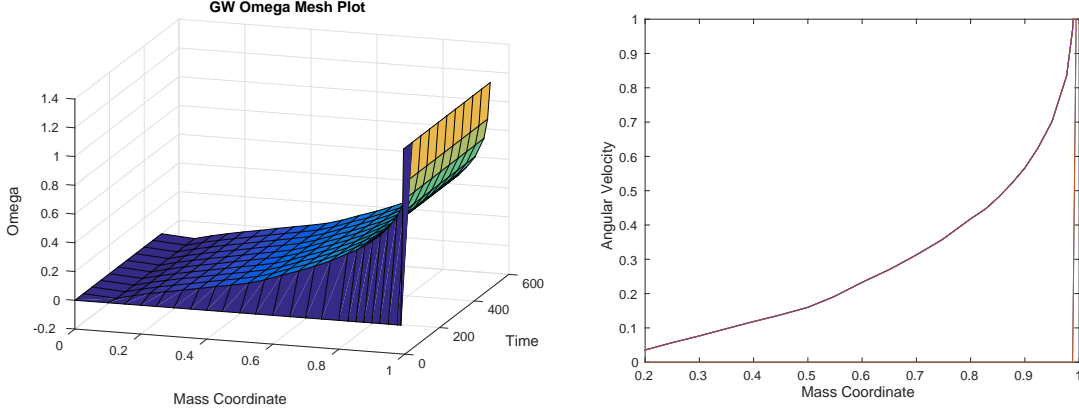


Fig. 3.— *Evolution of the angular velocity profile (in units of  $s^{-1}$ ) in the differential rotation case with KH and BC viscosities, and SN boundary condition (see text). The time axis is marked in units of the viscous timescale, the maximum time  $t_{max}$  being 500 in these units. Left Panel: 3-D surface plot. Right Panel: Stacked profiles in a 2-D plot, wherein the profiles at 10 equal time-steps are color coded, with time going up vertically.*

as the rapid attainment of the asymptotic profile makes the 10 equal time-step profiles completely indistinguishable from one another on this plot.

We now explore the effect of the YL boundary condition. We mimic this boundary condition by a simple prescription detailed in Appendix B, adequate for our purposes. Basically, as angular momentum is added to a non-rotating WD, the specific angular momentum at its surface,  $\ell_{surf}$ , increases according to the prescription

$$\frac{\partial \ell_{surf}}{\partial t} = \frac{\ell_K(R_{WD})}{t_{ac}}, \quad (13)$$

until the the angular velocity at the surface reaches the Keplerian value there. At that point, the surface angular velocity is maintained at the Keplerian angular velocity (which changes with time as accretion continues as the WD contracts). In Equation (13),  $\ell_K(R_{WD}) = \sqrt{GM_{WD}R_{WD}}$  is the Keplerian value of  $\ell$  at the surface of the WD of mass  $M_{WD}$  and radius  $R_{WD}$ . In reality, after the surface angular velocity reaches the Keplerian

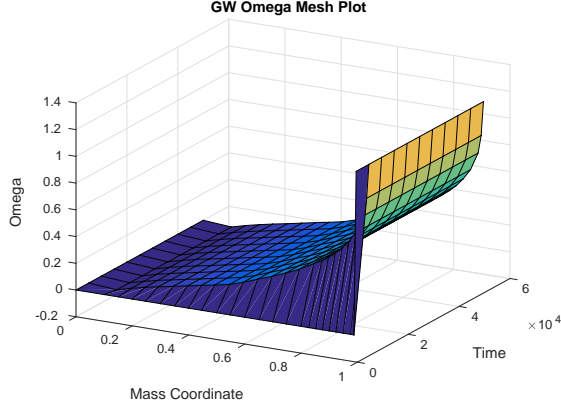


Fig. 4.— *Evolution of the angular velocity profile (in units of  $s^{-1}$ ) in the differential rotation case with KH and BC viscosities, and SN boundary condition (see text). The time axis is marked in units of the viscous timescale, the maximum time  $t_{max}$  being 50,000 in these units. Only the 3-D surface plot is shown in this case, for reasons explained in the text.*

value for the first time, the value of the Keplerian angular velocity at the surface increases as the WD contracts due to accretion, so that the actual surface angular velocity becomes sub-Keplerian, and so angular momentum is added to it by the accreting mass, spinning it to the Keplerian value again, and so on (Yoon & Langer 2004). This prescription is an adequate approximation for our purposes here.

In Figure 5, we show the evolution of the rotation profile with YL boundary condition and with a WD mass-radius relation described by a power-law index  $s = 1.2$  (see above), which roughly describes many of the computed WD models of Yoon and Langer (2004; see their Table 2). We follow the evolution to a maximum time  $t_{max} = 5000$  in the same units. We model the approach to Keplerian rotation at the surface by assuming that it is attained in a time  $t_K = 0.5t_{max}$  and maintained at Keplerian thereafter. As shown in Appendix B,  $t_K = x_c t_{ac} \approx t_{ac}$ , so that our choice corresponds to  $t_{ac} \approx 0.5t_{max} = 2500t_{visc}$  in this example. See further discussion below.

As Figure 5 shows, the asymptotic profile is obtained soon after Keplerian rotation is reached at the surface and changes little on further evolution.

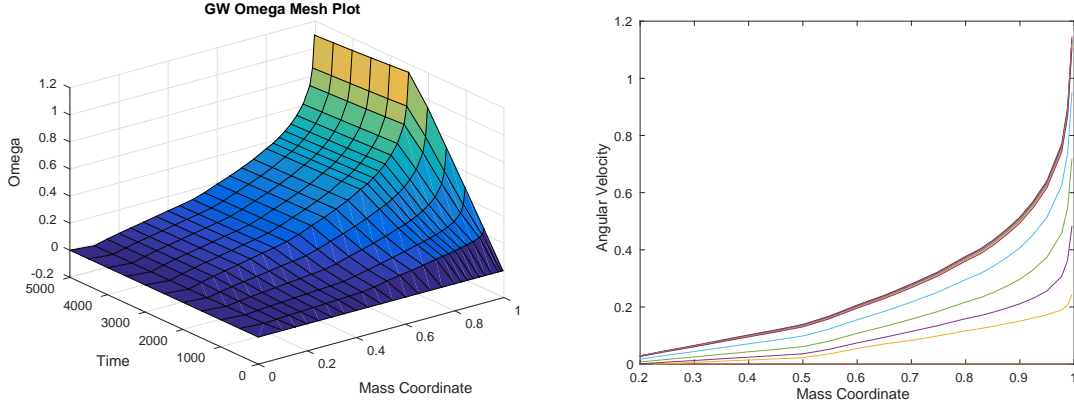


Fig. 5.— *Evolution of the angular velocity profile (in units of  $s^{-1}$ ) in the differential rotation case with KH and BC viscosities, and YL boundary condition, with a mass-radius relation with power-law index  $s = 1.2$  (see text). The time axis is marked in units of the viscous timescale, the maximum time  $t_{max}$  being 5000 in these units. Left Panel: 3-D surface plot. Right Panel: Stacked profiles in a 2-D plot, wherein the profiles at 10 equal time-steps are color coded, with time going up vertically.*

The evolutions shown in Figures 2, 3, 4, and 5 clarify the nature of the asymptotic rotation profile and demonstrate that SN or YL boundary conditions make little difference to the final profile. We stress at this point that we have used rather large values of  $t_{max} \sim 10^3 - 10^4$  in some of these calculations in order to simulate the effect of an accretion timescale  $t_{ac}$  which is much longer than the viscous timescale  $t_{visc}$  and demonstrate how the asymptotic profile is approached. For the large hydrodynamic viscosities generated by KHI and BCI, the actual value of  $t_{ac}/t_{visc}$  is much larger (see §7) and is not possible in practice to achieve computationally; however, the asymptotic approach shown above makes this unnecessary.

The profiles of the viscosities  $\nu_{\text{KH}}$  and  $\nu_{\text{BC}}$  (in cgs units) are shown in the left panel of Figure 6 for the asymptotic profile, calculated self-consistently during the computation. The viscosity is itself dependent on the  $\Omega$ -profile through the shear and hence the Richardson number (see §2.1). Shown in the right panel of the same figure are the profiles of the Richardson number  $\text{Ri}$  and its critical value  $\text{Ri}_{\text{BC}}$  defined in §2.1, for this asymptotic profile.

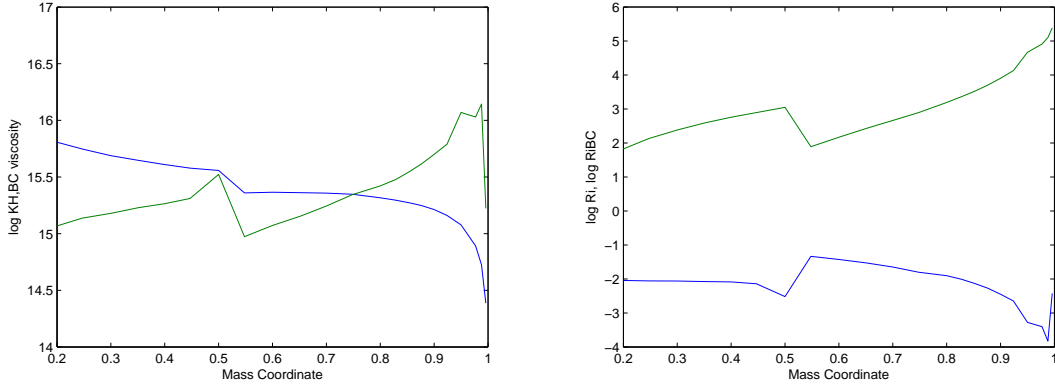


Fig. 6.— *Profiles of viscosity and Richardson number for the differential rotation case at the final time-step, calculated self-consistently during the run. Left Panel: logarithm of the KH and BC viscosities in cgs units. Color code: KH blue, BC green. Right Panel: logarithm of Ri and its critical value  $\text{Ri}_{\text{BC}}$  defined in §2.1. Color code: Ri blue,  $\text{Ri}_{\text{BC}}$  green.*

Figure 6 shows that the KH viscosity is comparable to or less than the BC viscosity throughout the structure. This suggests that the solution would not be significantly different if we were to neglect the BC viscosity and employ only the KH viscosity. We ran such models and, as expected, found a similar differentially-rotating solution. See §6 for a related discussion. Note from the right panel of Figure 6 that  $\text{Ri} \sim 10^{-2}$  in this solution, in strong contrast to the value  $\text{Ri} \sim 10^6$  found in the regime of nearly solid body rotation that had negligible KH viscosity, and an intermediate value of the BC viscosity.

## 5. Regime of Internal Rotation for Zahn Viscosity

The secular, low, Zahn viscosity (Equation (8)) produces a regime of differential rotation (Saio & Nomoto 2004). We show the evolution of the  $\Omega$ -profile as accretion proceeds for the case of Zahn viscosity in Figure 7. The left panel displays a 3-D surface plot and the right panel shows stacked profiles in a 2-D plot, as before. We stress that the viscous timescale  $t_{visc}$  in this low-viscosity case is generally comparable to the accretion timescale  $t_{ac}$ , a point we discuss in detail in §7. The time axis in Figure 7 is marked in units of the viscous timescale.

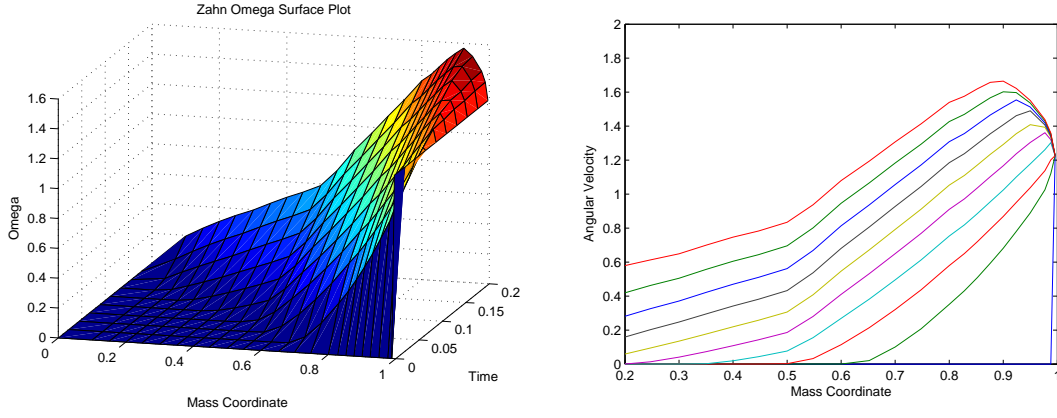


Fig. 7.— *Evolution of the angular velocity profile (in units of  $s^{-1}$ ) with Zahn viscosity. The time axis is marked in units of the viscous timescale, which is generally comparable to the accretion timescale for the Zahn viscosity. Left Panel: 3-D surface plot. Right Panel: Stacked profiles in a 2-D plot, wherein the profiles at 10 equal time-steps are color coded, with time going up vertically.*

The evolved Zahn profile has a characteristic maximum in  $\Omega$  in the outer parts of the WD, with  $\Omega$  decreasing with increasing  $r$  or  $M_r$  in those parts of the star beyond this maximum. The left panel of Figure 8 shows the profile of the Zahn viscosity  $\nu_Z$  (in cgs units) and the right panel that of the Richardson number,  $Ri$ , at the final time step,

calculated self-consistently during the computation. Note that  $Ri$  is in the low- $Ri$  regime as defined in this work. The viscosity in this case is also dependent on the shear, through the Richardson number, as in the high-viscosity case described earlier. Figure 8 shows that the Zahn viscosity falls in a typical range of  $10^2$  to  $10^4$   $\text{cm}^2\text{s}^{-1}$ , defined here as a regime of *low viscosity*.

We re-emphasize here that  $t_{visc}$  is generally of the same order as  $t_{ac}$  for the low Zahn viscosity. Accordingly, the picture presented in §4.2 for the situation  $t_{visc} \ll t_{ac}$ , wherein the rotation profile can be thought of as attaining an “asymptotic” shape quickly on the viscous timescale and that shape then evolving much more slowly on the accretion timescale, does not apply here. Instead, the whole profile evolves slowly on a common timescale  $\sim t_{visc} \sim t_{ac}$ . We return to this and related matters in §7.

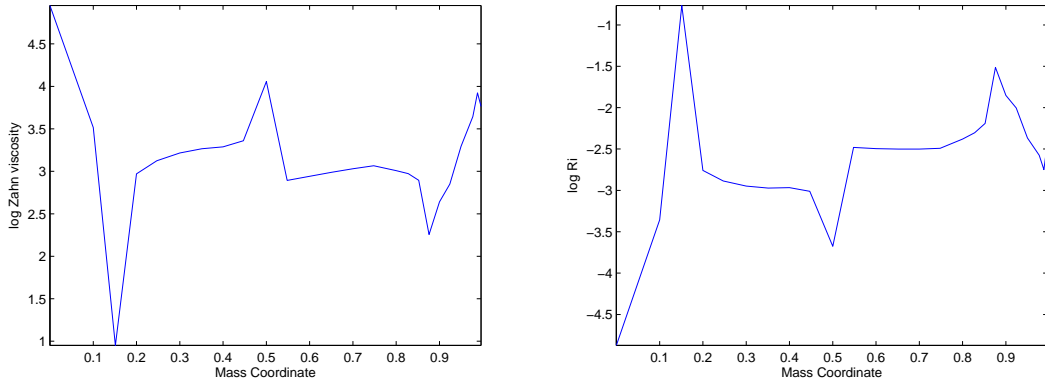


Fig. 8.— *Profiles of Zahn viscosity and Richardson number at the final time-step, calculated self-consistently during the run. Left Panel: logarithm of Zahn viscosity in cgs units. Right Panel: logarithm of the Richardson number  $Ri$ .*



## 6. The Yoon-Langer Regime

Yoon and Langer (2004, 2005, henceforth YL) studied internal rotation profiles of accreting white dwarfs in a pioneering study contemporaneous with that of Saio and Nomoto (2004). Among the high, hydrodynamic viscosities discussed in §2.1, these authors included KH viscosity, but not BC viscosity, arguing that it was unlikely to be operational inside WDs (see §2.1.2 and §8). YL also included the low, secular Zahn viscosity described in §2.2 and §5. These authors also included mechanisms we characterized in §2 as transporters of angular momentum in the  $\hat{\theta}$ -direction or horizontal direction, *viz.*, ES circulation and GSF instability. A typical rotation profile found by YL is shown in Figure 9.

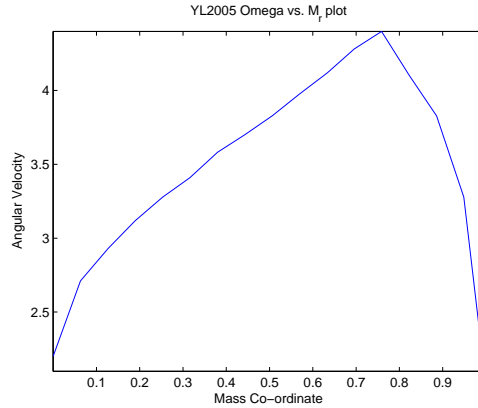


Fig. 9.— *Angular velocity profile of a typical YL model, showing differential rotation with a maximum in  $\Omega$  (in units of  $s^{-1}$ ) in the outer parts of the WD. From Yoon and Langer (2005).*

The YL profile has a characteristic maximum in  $\Omega$  in the outer parts of the WD, with  $\Omega$  decreasing with increasing  $r$  or  $M_r$  in those parts of the star beyond this maximum. At radii smaller than that corresponding to the maximum in  $\Omega$ , the angular momentum transport is dominated by the KH viscosity, with the Richardson number  $Ri$  maintained very close to its critical value of  $1/4$  (see §2.1.1) throughout almost all this inner region.

The effective viscosity in the inner regions of this solution is  $\nu_{KH} \sim 10^8$  and hence in the range of intermediate viscosity as defined here. At larger radii,  $Ri$  exceeds its critical value, KHI is shut off, and the radial angular momentum transport is dominated basically by the low Zahn viscosity, with ES and GSF processes (which generate low viscosities) being also operational.

The YL regime is thus a combination of two regions, one with intermediate viscosity and the other with low viscosity, as opposed to all other regimes described in earlier sections of this paper, which were governed either entirely by high viscosity, entirely by intermediate viscosity, or entirely by low viscosity. This leads to interesting consequences, which we discuss in §7.

## 7. Multiplicity of Regimes: General Discussion

We now give a general overview of the multiple rotation regimes for accreting WDs found so far, as described above, clarifying the current understanding of the origins of these regimes. Figure 10 gives a schematic summary of the regimes we summarize below.

We note first that three timescales are of crucial importance in this problem. The first, and by far the shortest, timescale is the viscous timescale for angular momentum penetration into the whole WD,  $t_{KHBC}$ , due to the large hydrodynamic viscosity,  $\nu_{KHBC}$ , generated by the combined action of KHI and BCI, as detailed in §2.1. Since the scale of this viscosity is very large,  $\nu_{KHBC} \sim 10^{15} - 10^{16} \text{ cm}^2 \text{ s}^{-1}$ , as seen from Figures 6 and 10, the viscous timescale, given by

$$t_{KHBC} \sim R_{WD}^2 / \nu_{KHBC} \sim (1 - 10) R_8^2 \text{ s} , \quad (14)$$

is very short. Here,  $R_8$  is  $R_{WD}$  in units of  $10^8 \text{ cm}$ .

The second, much longer timescale, is the viscous timescale for angular momentum

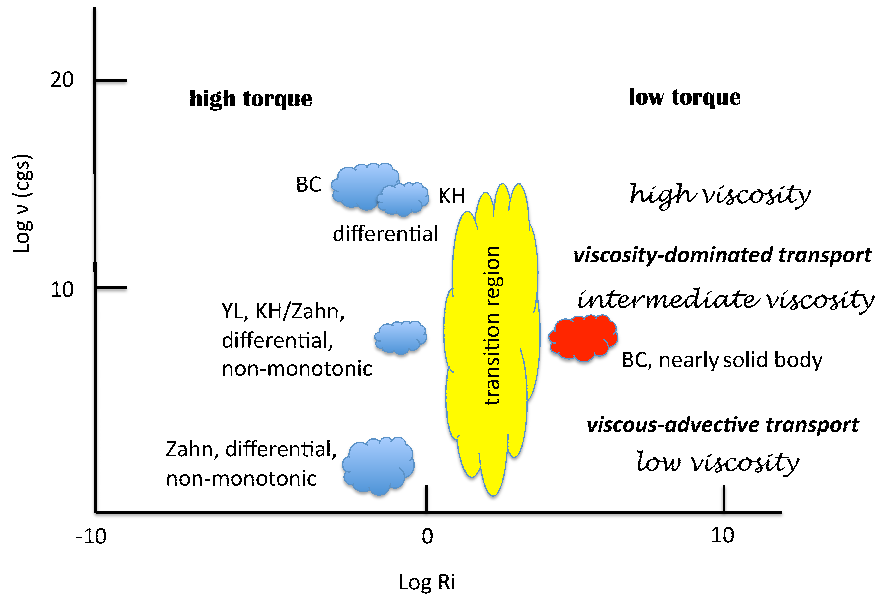


Fig. 10.— Schematic representation of the various regimes of rotational state presented in the plane of the log of effective viscosity versus the log of  $Ri$ .

penetration into the whole WD,  $t_Z$ , due to the low, secular, Zahn viscosity,  $\nu_Z$  described in §2.2. Since the scale of this viscosity is very low,  $\nu_Z \sim 10^1 - 10^4 \text{ cm}^2 \text{ s}^{-1}$ , as seen from Figures 8 and 10, the viscous timescale, given by

$$t_Z \sim R_{\text{WD}}^2 / \nu_Z \sim (10^{12} - 10^{15}) R_8^2 \text{ s} , \quad (15)$$

is very long.

The third timescale is that on which the advection effect, as detailed in §3, transports angular momentum into the whole WD. The timescale for this process is simply the accretion timescale,

$$t_{ac} \equiv \frac{M_{\text{WD}}}{\dot{M}_{\text{WD}}} \sim 10^{12} - 10^{14} \text{ s} \sim 10^5 - 10^7 \text{ yr} \quad (16)$$

in this problem. In the subsequent discussion, we take a representative value of  $10^{13} \text{ s}$  where required for explicit calculations.

We note that there is a huge separation between  $t_{KHBC}$  and  $t_{ac}$ , while there is a large overlap between  $t_Z$  and  $t_{ac}$ . A straightforward characterization of the rotation regimes that emerge from the interplay of these timescales can be given as follows.

Consider first the situation where the hydrodynamic viscosity is relevant. Then the viscous timescale,  $t_{KHBC}$ , determines the fast, viscous evolution, leading to an asymptotic profile that can be either nearly-uniform or strongly differential rotation depending on the operational regime of  $\text{Ri}$ , as detailed in §4. This profile subsequently evolves very slowly on the accretion timescale  $t_{ac}$ . We can call this situation the *viscosity-dominated* transport of angular momentum (Figure 10) subject to the caveats below.

The two regimes of rotation found in §4.1 and §4.2, *i.e.*, nearly-uniform and strongly differential rotation, arise from the fact that there are two regimes of BC viscosity, as shown by Equation (7) and illustrated in Figure 10, where the scalings of  $\nu_{\text{BC}}$  and the viscous stress,  $\tau$ , with the shear,  $\sigma$ , are quite different. The former regime is that of  $\text{Ri} < \text{Ri}_{\text{BC}}$ ,

which corresponds to strong differential rotation, and the latter that of  $\text{Ri} \gg \text{Ri}_{\text{BC}}$ , which corresponds to nearly-uniform rotation. Note that the viscous stress-shear relation is non-linear in both regimes, but the degree of non-linearity is different in the two regimes, with  $\tau$  scaling as  $\sigma^2$  in the former regime, but as  $\sigma^4$  in the latter. We emphasize that it is this difference in the degree of non-linearity that causes the two different regimes of rotation. A similar argument holds for  $\nu_{KH}$  in the regime of small  $\text{Ri}$ , in accord with Equation (4). For large values of  $\text{Ri}$ ,  $\nu_{KH}$  vanishes, of course, as the KHI shuts off.

A useful way of classifying these two regimes is obtained from considerations of angular momentum and torque introduced in §3 through Equations (9) and (11), when applied to the idea of the two-phase evolution of the  $\Omega$ -profile, first on the viscous then on the accretion timescale, for high hydrodynamic viscosities (see the beginning of §4.2). The profile first evolves on the short viscous timescale to an asymptotic, quasi-steady state that is described by the limit of Equation (9) where the left-hand side is approximately zero, which implies that  $\partial\Sigma/\partial r \approx 0$ , *i.e.*, a spatially-constant  $\Sigma$ . This asymptotic viscous state is thus one in which the total torque  $\Sigma$  is roughly a constant inside the white dwarf, which we can label  $\Sigma_0$ . As accretion proceeds on a much longer timescale, stellar conditions evolve slowly on this long accretion timescale, and  $\Sigma_0$  also evolves on the accretion timescale, corresponding to the slow evolution of the asymptotic profile on the accretion timescale.

The two regimes can now be described in terms of the two constant-torque asymptotic states in a straightforward way. Note first that the total torque  $\Sigma$  is given by Equation (11), the first term on the right-hand side being the viscous part and the second, the advective part. In the high-viscosity regime, the first term is normally dominant. Consider first the strong differential-rotation regime, where the shear is large,  $\text{Ri}$  is small, the viscosity is high, and the viscous term is thus completely dominant. Here the constant torque is given approximately by  $\Sigma_0 \approx 4\pi\rho r^4\nu(\partial\Omega/\partial r)$ , a large constant with a finite shear. Thus, there

is strong angular momentum transport in this asymptotic state, dominated by viscous transport. Consider next the nearly-uniform rotation regime, where the shear is small,  $Ri$  is large, and the viscosity takes an intermediate value as illustrated in Figure 10. Here, both viscous and advective components are small, and so, therefore, is the constant torque,  $\Sigma_0$ . In this small-torque regime, the angular momentum transport is very small, but non-vanishing.

A constant-torque solution corresponding to the asymptotic viscous profile is thus a generic feature of the high-viscosity regimes. The case where the constant,  $\Sigma_0$ , is very small is the nearly-uniform rotation regime, which does not appear to be otherwise special. We emphasize that a *strictly* constant- $\Omega$  solution is not possible, as there would be no viscous transport at all in that case: the shear would then be exactly zero, and so would be both the KH and the BC viscosities, as Equations (4) and (7) show.

A final remark about the hydrodynamic viscosities used in this work is that there may be caveats about their prescriptions that need to be studied further. We briefly consider here those relating to the BC viscosity. The widely-used Fujimoto prescription (Fujimoto 1993; Saio & Nomoto 2004; Piro 2008), as given by Equation (7), is obtained in the limit  $Ri \gg 1$  (Fujimoto 1993). For the regime of rotation profile described by Figure 6, however, this condition is not satisfied. In order to check the self-consistency of this regime, we have therefore gone back to the original Fujimoto (1988) prescription (see Equation (26) of that paper), which is more complicated but valid for general values of  $Ri$ , and calculated values of  $\nu_{BC}$  corresponding to the range of  $Ri$ -values shown in Figure 6. We have then compared these  $\nu_{BC}$ -values with those in Figure 6, obtained with the simple prescription of Equation (7). We have found that the full prescription gives  $\nu_{BC}$ -values that are smaller than those obtained from the simple prescription by factors that range between 2 and 5 over the entire range of  $Ri$ -values given in Figure 6. We recall now from §4.2 that the rotation profile in this

regime is determined by the sum of KH and BC viscosities, and that the two are generally comparable in value, with  $\nu_{\text{KH}}$  having a higher value over most of the star, as Figure 6 shows. Therefore, the rotation profile obtained with the more complicated BC-prescription will be qualitatively very similar to that obtained with the simpler prescription, although it will have a higher dominance of KH viscosity. Thus this regime is roughly self-consistent. We do not adopt the more complicated Fujimoto prescription of BC viscosity in this work because of other, more general, concerns about the BC viscosity (§8).

Consider now the situation when the secular Zahn viscosity is relevant, Figure 10. Since  $t_{ac} \sim t_Z$  over most of the phase space, viscosity and advection generally play comparable roles in angular momentum transport in this case. The result is a regime of differential rotation where the penetration of angular momentum into the interior of the WD is due to both viscosity and advection, the two terms being roughly comparable in magnitude over most of the WD interior. We call this situation the *viscous–advective* transport of angular momentum (Figure 10). Similar or related situations have been studied in other areas of physics and are sometimes called *advection–diffusion*.

Consider, finally, the YL regime that requires a detailed discussion because of its special, interesting nature, as indicated in §6. We show first that the hierarchy of timescales established at the beginning of this section also holds for the YL regime. This is so because the viscous timescale for angular momentum penetration into the WD,  $t_{\text{KH}}^{\text{YL}}$ , due to the large hydrodynamic viscosity  $\nu_{\text{KH}}^{\text{YL}}$  generated by KHI in the YL regime pertains in the inner regions of the WD. This regime of intermediate viscosity and short viscous time occurs at radii smaller than that at which  $\Omega$  has a maximum (this region covers roughly the inner  $\sim 80\%$  of the WD mass). The scale of  $\nu_{\text{KH}}^{\text{YL}} \sim 10^8 - 10^9 \text{ cm}^2 \text{ s}^{-1}$  can be seen in Figure 8 of Yoon and Langer (2004). This is quite large, although smaller than the high-viscosity scale associated with the regime of low Ri (Figure 10), and hence in the range of intermediate

viscosity as defined here. The reduction in viscosity is due to the fact that the Richardson number is very close to its critical value  $1/4$  (see Equations (4) and (5)) over this entire region of the YL regime. This value of the KH viscosity leads to a viscous timescale given by

$$t_{KH}^{YL} \sim R_{WD}^2 / \nu_{KH}^{YL} \sim (10^7 - 10^8) R_8^2 \text{ s} , \quad (17)$$

which can be compared with Zahn timescale  $t_Z$  and the accretion timescale  $t_{ac}$ , which are still given by Equations (15) and (16) respectively.

The nature of the YL regime can now be clarified in a straightforward way. As emphasized by these authors, although the inner region of their regime does have a large, hydrodynamic viscosity and so a rapid viscous transport, the low Zahn viscosity in their outer region with its slow transport (with a comparable contribution from advection) represents a severe “bottleneck” in the angular momentum transport into the WD interior (Yoon & Langer 2004). It could be argued, therefore, that overall penetration of the accreted angular momentum into the WD can only happen on the long timescale  $\sim t_{ac} \sim t_Z$ . One could then argue further that the Zahn and YL regimes are rather similar in this sense, and cite the general similarity between the shapes of the Zahn and YL  $\Omega$ -profiles (even to the extent that the maximum in  $\Omega$  comes in the range  $\sim 80 - 90\%$  of the WD mass in both cases) in support of this point of view. Strictly speaking, however, this is not correct because there is provision for fast viscous transport in the YL case in the deep interior of the WD, once the angular momentum reaches there. Indeed, in analogy with the discussion given earlier, the question of a possible “asymptotic profile” in this interior YL region merits detailed study, but is outside the scope of this paper.

We thus see that, among the multiple regimes of rotation described above, many possible regimes of differential rotation exist, in addition to that of uniform rotation. Indeed, it appears that the *generic* regime is one of differential rotation and the uniform



rotation regime may be a special case.

## 8. Discussion and Conclusions

We have attempted to clarify the nature of the different regimes of internal rotation that can exist inside accreting WDs. We consider WDs without strong, permanent magnetic fields and hence consider angular-momentum transport processes described by viscosities generated by hydrodynamic mechanisms such as Kelvin–Helmholtz and baroclinic instabilities, and secular mechanisms such as the Zahn instability. We formulated these viscosities with the aid of prescriptions given in the literature.

We elucidate that the BC viscosity as adopted here implies two asymptotic regimes depending on the Richardson number,  $Ri$ . The BC viscosity,  $\nu_{BC}$ , scales as  $Ri^{-1/2} \propto \sigma$  in the regime of small  $Ri$ . This yields a regime of high viscosity that nevertheless corresponds to differential rotation, a solution presented here for the first time. The BC viscosity scales as  $Ri^{-3/2} \propto \sigma^3$  in the regime of large  $Ri$ , yielding an intermediate level of viscosity and solid-body rotation.

We thus classify the collection of rotation regimes explored here in terms of the Richardson number,  $Ri$ , in the following way. At small values of  $Ri \lesssim 0.1$ , we have both the low-viscosity Zahn regime and the new, high-viscosity regime found in this work. Near the critical value of  $Ri \approx 1/4$ , we have the inner, intermediate-viscosity region of the YL regime, its outer, low-viscosity region being at a higher value of  $Ri$ . Employment of KH viscosity alone yields differential rotation. Finally, at large values of  $Ri \gg 1$ , we have the intermediate-viscosity nearly-uniform rotation regime.

The two regimes of the BC viscosity correspond to a viscosity that scales with the shear as  $\sigma$  in the small  $Ri$  regime and as  $\sigma^3$  in the large  $Ri$  regime (§2.1.2). This implies,

in turn, that the viscous stress,  $\tau = \nu\sigma$ , scales with the shear as  $\sigma^2$  in the small Ri regime, but as  $\sigma^4$  in the large Ri regime. The form of nonlinearity is a power-law with an index  $n > 1$ ,  $n$  being 2 in the small Ri regime, and 4 in the large Ri regime. It is interesting to consider what the situation would be in a more complete theory of BC viscosity. Instead of the knowledge of  $\nu_{\text{BC}}$  only in the two limits  $\text{Ri} < \text{Ri}_{\text{BC}}$  and  $\text{Ri} \gg \text{Ri}_{\text{BC}}$ , we would then have a complete prescription over the whole range of Ri, which would reduce to the above limits appropriately. The non-linearity in the viscous stress will change from a power-law with  $n = 2$  to one with  $n = 4$  as Ri increases, and the rotation regime will change from a strongly differential to nearly-uniform. Accordingly, the two limiting regimes will have a *transition region* between them, as illustrated schematically in Figure 10.

An insight that is particularly useful for our problem in the regimes of power-law viscosities is available from the literature on the p-Laplacian nonlinear diffusion equation (Kamin & Vazquez 1988; Lee et al. 2006; Bidaut-Veron 2006; Akagi & Matsuura 2013), whose form,  $\partial u / \partial t = \nabla \cdot (|\nabla u|^{p-2} \nabla u)$ , is very similar to that of Equation (12) in the limit where viscous transport dominates over advective transport, as is the case for the large hydrodynamic viscosities. This similarity becomes clear if the advective term in Equation (12) is neglected and the equation is rewritten back in terms of the angular velocity  $\Omega$  to read  $\partial \Omega / \partial t = (1/\rho r^4)(\partial / \partial r)(\rho r^4 \nu (\partial \Omega / \partial r))$ . The power-law index  $n$  for the viscous stress  $\nu\sigma$  is related to the index  $p$  by  $n = p - 1$ , so that that the two asymptotic regimes correspond to  $p = 3$  and  $p = 5$ , respectively.

The non-trivial asymptotic solution of the p-Laplacian PDE for a *given* value of  $p$  can be shown to be unique, but the solutions for *different* values of  $p$  are quite different (Kamin & Vazquez 1988; Lee et al. 2006). This is consistent with the two viscosity regimes found here. The implication is that when  $p$  changes from one value to another through the transition region, the solution will undergo a corresponding transition. The

specific issue of the behavior of the BC viscosity at such intermediate  $p$ - or  $n$ -values (or, equivalently, the corresponding values of  $Ri$ ) are beyond the scope of this paper, but of definite interest.

There has been discussion in the literature about the applicability of BCI in the electron-degenerate matter inside WDs since completely degenerate matter is barotropic, pressure is only a function of density and their gradients cannot be skew to one another (Kippenhahn & Mölenhoff 1974; Tassoul 1984; Yoon & Langer 2004). Realistic WDs have finite temperature so the issue of baroclinicity is a quantitative one. The key point is that buoyancy may become very small in degenerate matter, with consequences for  $Ri$  and other parameters of the problem, in which case the standard BCI formulation, including the Fujimoto prescription, may not apply. A first-principles reformulation of the problem may be necessary.

While our immediate goal in this work has been to better understand the physics that drives the differential rotation regimes of accreting white dwarfs, our larger, long-term goal is to elucidate the progenitor evolution of SN Ia. Currently viable models of SN Ia involve either accretion onto a WD from a non-degenerate star (the SD scenario), from a degenerate companion (the DD scenario), or the violent impact of two degenerate stars (Maoz, Mannucci & Nelemans 2014). All these possibilities demand that the WD progenitor of the SN Ia be rotating. It is an interesting task to use the physics of angular momentum transport described here to elucidate and guide our understanding of the possible rotation state of the progenitors of SN Ia. A major challenge remains to determine what rotational states nature accommodates, under what circumstances, and to what effect on the subsequent explosion.

The reverse problem, *viz.*, using observations of SN Ia to constrain the physics of the progenitor evolution, is equally interesting and perhaps even more challenging. While

acknowledging the definite variety among typical SN Ia, we must recognize that the majority of these events display a remarkable degree of homogeneity. The fact that most SN Ia are consistent with values of ejecta mass not remarkably different from  $M_{\text{Ch}}$  suggests that most SN Ia cannot be in a regime of strong differential rotation, neither that of low  $\text{Ri}$  we have presented here nor in the regime propounded by Yoon & Langer (2004). Thus, it is important to understand the conditions that prevent regimes of differential rotation from occurring in common circumstances. The answer cannot be so simple as saying that the viscosity, even magnetic viscosity, is large, because we have shown here that there can be differential rotation in a high-viscosity regime. Likewise, some SN Ia fall in the Super-Chandrasekhar regime that would seem to demand differential rotation, implying that the nearly solid-body rotation solutions of Saio & Nomoto (2004) and of Piro (2008) do not pertain. If many SN Ia involve sub-Chandra masses, as suggested by Scalzo et al. (2014) and others, then the state of rotation is currently unconstrained. The nature of internal rotational profiles in all these circumstances requires deeper understanding.

We thank Michael Montgomery for providing the basic white dwarf model and for helpful discussion of white dwarf structure and the referee for helpful comments which improved the paper. Some work on this paper was done in the hospitable environment of the Aspen Center for Physics that is supported by NSF Grant PHY-1066293. P. G. thanks the University of Texas at Austin for its warm hospitality during part of this work. The authors are also grateful for the Posse East establishment where much of the conceptual development of this work was done. This work was supported in part by NSF Grant NSF AST-1109801.

### A. The Advection Effect

In modeling the inward mass advection rate  $\dot{M}(r, t)$  in the interior of the WD, we first note that, due to mass conservation inside the WD, we can express the advection rate as

$$\dot{M}(r, t) = \dot{M}_r(r, t), \quad (\text{A1})$$

in terms of the mass co-ordinate  $M_r$  introduced in §3, and defined by

$$M_r = \int_0^r 4\pi\rho(r, t)r^2 dr. \quad (\text{A2})$$

We must then model  $\dot{M}_r$  for accreting WDs in terms of the accretion rate  $\dot{M}_{WD}$  on the WD, or, equivalently, model  $\dot{M}_r/M_r$  in terms of  $\dot{M}_{WD}/M_{WD}$ .

For the simple case of a uniform density profile, it is trivial to show that

$$\frac{\dot{M}_r}{M_r} \propto \frac{\dot{M}_{WD}}{M_{WD}}. \quad (\text{A3})$$

For approximately self-similar contraction of the WD as its mass increases, *i.e.*, a contraction during which the density profile remains roughly self-similar, Equation (A3) still holds approximately, with the constant of proportionality replaced by a slowly-varying function of radius. The value of this function varies by a factor  $\sim 1$  between the center and the surface of the star, so that Equation (A3) is approximately valid over the entire extent of the WD. This means that  $\dot{M}_r/M_r$  is roughly independent of radius and roughly proportional to  $\dot{M}_{WD}/M_{WD}$ . In other words, the dominant radial variation in  $\dot{M}_r$  is given by that in  $M_r$ ; detailed structure effects give only a slow variation.

We illustrate this point with polytropic models, used widely in studies of WDs. A polytrope with polytropic index  $n$  has an equation of state  $p = K\rho^{1+1/n}$ , and a density profile  $\rho = \rho_c\theta^n$ , where  $\theta(\xi)$  is the Lane-Emden function of index  $n$ . Here,  $\rho_c$  is the central density, and the scale,  $a$ , used to define the dimensionless radial co-ordinate

$$\xi \equiv r/a \quad (\text{A4})$$

inside the polytrope is given by

$$a \equiv \left[ \frac{(n+1)K\rho_c^{\left(\frac{1}{n}-1\right)}}{4\pi G} \right]^{1/2}. \quad (\text{A5})$$

The mass of the polytropic WD is given by

$$M_{\text{WD}} \equiv 4\pi \left[ \frac{(n+1)K}{4\pi G} \right]^{3/2} \rho_c^{\frac{3-n}{2n}} \xi_1^2 | \theta'(\xi_1) |, \quad (\text{A6})$$

and its radius by  $R_{\text{WD}} = a\xi_1$ . Here,  $\xi_1$  is the value of  $\xi$  at the surface of the polytrope (where the density is zero), and  $\theta'(\xi_1)$  is the value of the derivative of  $\theta$  at  $\xi_1$ . Tables of  $\xi_1$  and  $| \theta'(\xi_1) |$  for various values of  $n$  are widely available.

The value of  $M_r$ , as given by Equation (A2), can be readily calculated with the aid of the equations given in the previous paragraph, and this value can be related to  $M_{\text{WD}}$  as given by Equation (A6) to obtain

$$M_r = \frac{M_{\text{WD}}\phi(\xi, n)}{\xi_1^2 | \theta'(\xi_1) |}. \quad (\text{A7})$$

Here,

$$\phi(\xi, n) \equiv \int_0^\xi \theta^n(\xi) \xi^2 d\xi \quad (\text{A8})$$

is an appropriate moment of the Lane-Emden function  $\theta$ .

Equation (A7) allows us to calculate the left-hand side of Equation (A3) for the polytropic case as

$$\frac{\dot{M}_r}{M_r} = \frac{\dot{M}_{\text{WD}}}{M_{\text{WD}}} + \frac{\dot{\phi}}{\phi}. \quad (\text{A9})$$

The second term on the right-hand side of Equation (A9) can be evaluated with the aid of Equations (A8) and (A4) as

$$\frac{\dot{\phi}}{\phi} = -\frac{\theta^n(\xi)\xi^3}{\phi} \left( \frac{\dot{a}}{a} \right). \quad (\text{A10})$$

The relation between the total mass,  $M_{\text{WD}}$ , and the radius scale,  $a$ , for a polytrope of index  $n$  is well-known to be

$$M_{\text{WD}}.a^{\left(\frac{3-n}{n-1}\right)} = \text{constant}, \quad (\text{A11})$$

and can be derived by combining Equations (A5) and (A6), the constant in the above equation coming out to be  $4\pi \left[ \frac{(n+1)K}{4\pi G} \right]^{\frac{n}{n-1}} \xi_1^2 | \theta'(\xi_1) |$ . Equation (A11) is closely related to the mass-radius relation for polytropes. A logarithmic differentiation of it yields

$$\frac{\dot{a}}{a} = - \left( \frac{n-1}{3-n} \right) \frac{\dot{M}_{WD}}{M_{WD}}. \quad (\text{A12})$$

Combining Equations (A9), (A10), and (A12), we arrive at the final result:

$$\frac{\dot{M}_r}{M_r} = \frac{\dot{M}_{WD}}{M_{WD}} g_n(\xi), \quad (\text{A13})$$

where the function  $g_n(\xi)$  is defined by

$$g_n(\xi) \equiv 1 + \left( \frac{n-1}{3-n} \right) \frac{\theta^n(\xi) \xi^3}{\phi(\xi, n)}. \quad (\text{A14})$$

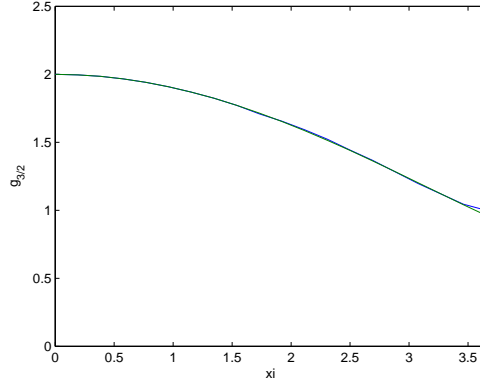


Fig. 11.— *The function  $g_{3/2}(\xi)$  for  $n = 3/2$  polytropes. Note that the surface of the polytrope (where the density falls to zero) corresponds to  $\xi = \xi_1 \approx 3.654$  for this value of the polytropic index. Blue line: Exact calculation. Green line: Taylor approximation.*

The function  $g_{3/2}(\xi)$  for the polytropic index  $n = 3/2$ , often used in model WD calculations, is shown in Figure 11. It is a slowly-varying function, increasing from unity at the surface of the polytrope to a value of 2 at the center. For comparison, we have used a

Taylor expansion of the Lane-Emden function of polytropic index  $n$ , which is given by

$$\theta_n(\xi) = 1 - \frac{1}{6}\xi^2 + \frac{n}{120}\xi^4 - \frac{n(8n-5)}{15120}\xi^6 + \dots, \quad (\text{A15})$$

to derive a series representation of  $g_n$ , the result being

$$g_n(\xi) = 1 + \frac{3(n-1)}{3-n} \left[ 1 - \frac{n}{15}\xi^2 + \frac{n(19n-25)}{3150}\xi^4 - \dots \right], \quad (\text{A16})$$

which reduces in the special case  $n = 3/2$  to

$$g_{3/2}(\xi) = 2 - \frac{\xi^2}{10} + \frac{\xi^4}{600} - \dots \quad (\text{A17})$$

This Taylor approximation to  $g_{3/2}(\xi)$  is also shown in Fig.11, keeping only the terms given in Equation (A17), and showing thereby how close this approximation is to the exact value.

Similar results are obtained for other polytropic indices, leading us to use the approximation for the advection rate given by Equation (10) in §3.

## B. YL Boundary Condition: A Simple Prescription

As explained in §4.2, we envisage angular momentum being added to a non-rotating WD, so that the specific angular momentum at its surface,  $\ell_{surf}$ , increases according to the prescription

$$\frac{\partial \ell_{surf}}{\partial t} = \frac{\ell_K(R_{WD})}{t_{ac}}, \quad (\text{B1})$$

where

$$\ell_K(R_{WD}) = \sqrt{GM_{WD}R_{WD}} \quad (\text{B2})$$

is the Keplerian value of  $\ell$  at the surface of the WD of mass  $M_{WD}$  and radius  $R_{WD}$ . We emphasize that both  $M_{WD}$  and  $R_{WD}$  here are functions of time as accretion goes on, which is of crucial importance in the relations given below.



We use the mass-radius relation

$$R_{\text{WD}} \propto M_{\text{WD}}^{-s} \quad (\text{B3})$$

introduced in §3, and describe the mass increase due to accretion by

$$M_{\text{WD}} = M_0 \left( 1 + \frac{t}{t_{\text{ac}}} \right), \quad (\text{B4})$$

$M_0$  being the initial mass of the WD, and  $R_0$  its initial radius.

Combining Equations (B1), (B2), (B3), and (B4), and integrating with respect to time, we obtain the dimensionless specific angular momentum at the surface,  $\lambda_{\text{surf}} \equiv \ell_{\text{surf}}/\ell_0$  in terms of the fiducial value  $\ell_0 \equiv \sqrt{gM_0R_0}$ , as a function of time in the form

$$\lambda_{\text{surf}}(t) = \frac{2}{3-s} \left[ (1+x)^{\frac{3-s}{2}} - 1 \right] \quad (\text{B5})$$

Here,  $x \equiv t/t_{\text{ac}}$  is a dimensionless time, in units of the accretion timescale. The surface angular velocity,  $\Omega_{\text{surf}} = \ell_{\text{surf}}/R_{\text{WD}}^2$  is similarly given in terms of the fiducial value  $\Omega_0 \equiv \sqrt{GM_0/R_0^3}$  as

$$\frac{\Omega_{\text{surf}}(t)}{\Omega_0} = \frac{2}{3-s} (1+x)^{2s} \left[ (1+x)^{\frac{3-s}{2}} - 1 \right]. \quad (\text{B6})$$

The above increase with time continues until the the angular velocity at the WD surface reaches the *instantaneous* Keplerian value  $\Omega_K R_{\text{WD}} \equiv \sqrt{GM_{\text{WD}}/R_{\text{WD}}^3}$  there. This happens when the ratio

$$\omega_{\text{surf}}(t) \equiv \frac{\Omega_{\text{surf}}(t)}{\Omega_K(R_{\text{WD}})} = \frac{2}{3-s} (1+x)^{\frac{s-1}{2}} \left[ (1+x)^{\frac{3-s}{2}} - 1 \right]. \quad (\text{B7})$$

reaches unity, which occurs at a critical value of the (dimensionless) time  $x_c$  given by the solution of the equation

$$x - (1+x)^{\frac{s-1}{2}} = \frac{1-s}{2}. \quad (\text{B8})$$

For values of  $s$  in the range  $\sim 1 - 2$ , as is the case for some actual WD models in the literature (see §9), the value of  $x_c$  is close to 1, as can be easily verified.

Beyond this point, the surface angular velocity is maintained at the current Keplerian angular velocity, *i.e.*,  $\omega_{surf}$  is maintained at a value of unity. Since the ratio of  $\lambda_{surf}(t)$  to  $\omega_{surf}(t)$  is seen to be

$$\frac{\lambda_{surf}(t)}{\omega_{surf}(t)} = (1+x)^{\frac{1-s}{2}} \quad (\text{B9})$$

by combining Equations (B5) and (B7), it follows that, under these circumstances,  $\ell_{surf}$  is given as a function of time by

$$\lambda_{surf}(t) = (1+x)^{\frac{1-s}{2}}. \quad (\text{B10})$$

## REFERENCES

- Akagi, G., & Matsuura, K. 2013, *Nonlinear Differential Equations & Applications NoDEA*, 20, 37.
- Bidaut-Veron, M. F. 2006, *Advanced Nonlinear Studies*, 6, 69.
- Charpinet, S., Fontaine, G., and Brassard, P. 2009, *Nature*, 461, 501.
- Chiosi, E., Chiosi, C., Trevisan, P., Piovan, L., & Orio, M. 2014, arXiv:1409.1104
- Dan, M., Rosswog, S., Brüggen, M., & Podsiadlowski, P. 2014, *MNRAS*, 438, 14
- Di Stefano, R., Voss, R., & Claeys, J. S. W. 2011, *ApJ*, 738, L1
- Di Stefano, R., & Kilic, M. 2012, *ApJ*, 759, 56
- Fink, M., Röpke, F. K., Hillebrandt, W., et al. 2010, *A&A*, 514, A53
- Fujimoto, M. Y. 1988, *A&A*, 198, 163.
- Fujimoto, M. Y. 1993, *ApJ*, 419, 768.
- Hachisu, I. 1986, *ApJS*, 61, 479.
- Hachisu, I., Tohline, J. E., and Eriguchi, Y. 1988, *ApJS*, 66, 315.
- Hachisu, I., Kato, M., Saio, H., and Nomoto, K. 2012, *ApJ*, 744, 69.
- Heger, A., Langer, N., and Woosley, S. E. 2000, *ApJ*, 528, 368.
- Hicken, M., *et al.* 2007, *ApJ*, 444, 363.
- Hillebrandt, W., *et al.* 2013, *Frontiers of Physics*, 8, 116.
- Howell, D. A., *et al.* 2006, *Nature*, 443, 308.

- Howell, D. A. 2011, *Nature Communications*, 2, 2.
- Ilkov, M., & Soker, N. 2013, *MNRAS*, 428, 579
- Imamura, J. N., *et al.* 1995, *ApJ*, 444, 363.
- Ji, S., Fisher, R. T., García-Berro, E., *et al.* 2013, *ApJ*, 773, 136
- Justham, S. 2011, *ApJ*, 730, L34
- Kagan, D., & Wheeler, J. C. 2014, *ApJ*, 787, 21
- Kamin, S., & Vazquez, J. L. 1988, *Revista Matematica Iberoamericana*, 4, 339
- Kippenhahn, R., & Möllenhoff, C. 1974, *Ap&SS*, 31, 117
- Kushnir, D., Katz, B., Dong, S., Livne, E., & Fernández, R. 2013, *ApJ*, 778, L37
- Lee, K.-A., Petrosyan, A., and Vazquez, J. L. 2006, *Journal Diff. Equation*, 229, 389
- Livio, M., & Riess, A. G. 2003, *ApJ*, 594, L93
- Maoz, D., Mannucci, F., & Nelemans, G. 2014, *ARA&A*, 52, 107
- Meng, X., & Podsiadlowski, P. 2013, *ApJ*, 778, L35
- Montgomery, M. H. 2010, private communication.
- Ostriker, J. P., and Bodenheimer, P. 1968, *ApJ*, 151, 1089.
- Pakmor, R., Kromer, M., Taubenberger, S., *et al.* 2012, *ApJ*, 747, L10
- Patat, F., Höflich, P., Baade, D., *et al.* 2012, *A&A*, 545, A7
- Piro, A. L. 2008, *ApJ*, 679, 616.
- Saio, H., and Nomoto, K. 2004, *ApJ*, 615, 444.

- Scalzo, R. A., *et al.* 2010, ApJ, 713, 1073.
- Scalzo, R., Aldering, G., Antilogus, P., *et al.* 2014, MNRAS, 440, 1498
- Silverman, J. M. *et al.* 2011, MNRAS 410, 585.
- Shen, K. J., & Moore, K. 2014, arXiv:1409.3568
- Spruit, H. C. 2002, A&A, 381, 923.
- Tassoul, J. L. 1984 in Proc. IAU Symp. 105, eds. A. Maeder & A. Renzini, (Dordrecht; Kluwer)
- Taubenberger, S., *et al.* 2011, MNRAS, 412, 2735.
- Tornambé, A., & Piersanti, L. 2013, MNRAS, 431, 1812
- Wang, B., & Han, Z. 2012, New A Rev., 56, 122
- Wheeler, J. C., *et al.*, in preparation.
- Woosley, S. E., & Kasen, D. 2011, ApJ, 734, 38
- Yamanaka, M., *et al.* 2009, ApJ, 707, L118.
- Yoon, S.-C., and Langer, N. 2004, A&A, 419, 623.
- Yoon, S.-C., and Langer, N. 2005, A&A, 435, 967.
- Zahn, J.-P. 1992, A&A, 265, 115.